INL-RPT-22-68987
Revision 0

CFD-Chemical Model of One-Third Scale Demonstration of DOE Sealed Canister with ATR Fuel

September 2022

Alexander W Abboud

Changing the World's Energy Future

INL-RPT-22-68987
Revision 0

CFD-Chemical Model of One-Third Scale Demonstration of DOE Sealed Canister with ATR Fuel

Alexander W Abboud

September 2022

Idaho National Laboratory
Idaho Falls, Idaho 83415

http://www.inl.gov

Prepared for the
U.S. Department of Energy
Office of Environmental Management
Under DOE Idaho Operations Office
Contract DE-AC07-05ID14517

Page intentionally left blank

SUMMARY

Road-ready and final disposition packaging configurations for the advanced test reactor (ATR) fuel currently plans for storage within helium-backfilled DOE sealed standard canisters. The aluminum cladding of the ATR fuel contains an oxyhydroxide layer of boehmite/bayerite that generates hydrogen when subjected to gamma radiation. Understanding the effect of this hydrogen buildup over time is important for long term storage considerations. Previous modeling efforts have built a coupled CFD-chemical model to simulate the temperature and gas phase concentrations within the DOE sealed standard canisters. A demonstration case for these DOE sealed canisters will be eventually performed with a one-third scale mockup with an instrumented lid containing thermocouples and gas sampling probes. This study models the demonstration canister for future validation of CFD-chemical, such that confidence in the model's long-term prediction for the full-scale system can be increased.

The deployment of the instrumented lid for online monitoring is intended for a period of 10+ years based on previous monitoring of commercial fuel storage; however, the model is still run for the previously used 50-year storage periods. This case is modeled with a G-value using a bi-linear function such that it decreases at higher dose rates to be consistent with mini-canister experiments. Validation efforts of the model would likely revolve around the results for the first couple of years, so the results of this timeframe are highlighted. For dried fuel of the nominal decay heat (18W), the predicted hydrogen concentration is 0.19% after 1 year, 0.91% after 10 years, and 2.8% after 50 years, with a maximum pressure of 1.26 atm.

As with previous modeling, the decay heat of the fuel is the main factor that influences the results. For dried fuel in pure helium the hydrogen concentration with changing decay heat ranges from 0.06% to 0.34% after 1 year, 0.35-2.11% after 10 years and 0.95 to 6.6% after 50 years. For undried fuel in pure helium, the hydrogen concentration ranges from 0.23 to 1.2% after 1 year, 1.25-6.2% after 10 years and 8.8 to 18.84% after 50 years. The maximum absolute pressure that is reached across any scenario is 2.06 atm. While long-term results with the presence of residual air are mostly the same, early reactions with O_2 can delay significant production of H_2 until it is consumed to form additional water vapor, lowering the hydrogen range. In the event of residual air, the presence of nitric acid is possible in the range of 18-131 ppm after 1 year, 174-1180 ppm after 10 years, and 586-3500 ppm after 50 years, depending on decay heat. The model predicts only trace amounts of oxygen across all scenarios. As long as the fuel is sufficiently dried, or of nominal decay heat, the 4% lower flammability limit of hydrogen will not be reached within a 10-year monitoring period.

ACKNOWLEDGEMENTS

This work was funded by the U.S. Department of Energy Environmental Management office. This work was performed by Battelle Energy Alliance, LLC, under DOE Idaho Operations Contract DE-AC07-05ID14517 and made use of the resources of the High Performance Computing Center at Idaho National Laboratory which is supported by the Office of Nuclear Energy of the U.S. DOE and the Nuclear Science User Facilities.

CONTENTS

FIGURES

TABLES

Page intentionally left blank

ACRONYMS

ATR	Advanced Test Reactor
ASNF	Aluminum-clad Spent Nuclear Fuel
CFD	Computational Fluid Dynamics
DOE	Department of Energy
INL	Idaho National Laboratory
SRNL	Savannah River National Laboratory
SNF	Spent Nuclear Fuel

Page intentionally left blank

CFD-Chemical Model of One-Third Scale Demonstration of DOE Sealed Canister with ATR Fuel

1. Introduction

By the year 2035, there will be ~2500 MTHM of spent nuclear fuel (SNF) that will require geologic repository disposal that is managed by DOE. Approximately 400 MHTM of this is currently not packaged (SNFWG, 2017). Previous studies in support of geologic disposal divided the DOE SNF inventory into 34 groups based on fuel matrix, cladding, cladding condition, and enrichment (SNFWG, 2017). The six aluminum clad fuel types are of interest as aluminum is significantly less corrosion resistant than stainless steel and zircaloy clad fuel. The aluminum cladding develops a corrosion layer that generates hydrogen from radiolysis, and can also contain bound, both physiosorbed and chemisorbed, water.

Over 30% of the volume of DOE stored fuel is aluminum clad. One source of the aluminum spent nuclear fuel (ASNF) that will continue to be produced and needs to be stored is the advanced test reactor (ATR) fuel at the Idaho National Laboratory (INL). The disposition path for this ASNF is to be loaded into road-ready DOE sealed standard canisters backfilled with helium for transportation and eventual long-term storage. A previous report examined the chemical contents within these DOE canisters using a set of radiolytic chemistry reactions for both the gas and the aluminum surface. The previous report utilized G-values for the surface reactions in an argon atmosphere, but recent experimental tests have shown that a helium environment has higher hydrogen generation rates (Parker-Quaife and Horne, 2021). These tests also show deviation from linearity with increasing dose, indicating a potential steady-state H_2 concentration, though higher dose samples are to be evaluated. Follow up tests have been completed which show the roll-over effect at high doses (Horne et al., 2022; Verst 2022), though do not appear to conclude a true steady state condition is reached for the 6061 alloy samples. This data was used to modify the previous chemical model to address this effect (Abboud 2022). The surface chemistry model currently uses a bi-linear function for the G-value as a function of total dose and is consistent with mini-canister test data.

As part of studying the safety for road ready packaging and long-term storage of ASNF, a demonstration case will likely occur in the future. This scenario is a one-third scale of the full-sized DOE sealed standard canister with a series of thermowells and gas sampling measurements inserted via an instrumented lid design. This study creates a CFD-thermal model of this setup, such that the temperature field can be compared with the measurements, and the coupled Cantera chemical model is used to predict hydrogen concentration rates over the monitoring period of the demonstration. This data will be used for eventual validation of the model to provide confidence for the safety of long-term storage of DOE sealed canisters loaded with ATR fuel.

2. Theory and Model Description

2.1 Thermal Fluid Model

The commercial multiphysics modeling platform STAR-CCM+ is used for modeling the canister (Siemens, 2022). The numerical solver implemented here is a finite-volume approach with second-order implicit time stepping and a second-order discretization scheme. The segregated flow solver for the Navier-Stokes equations is used, which is applicable to constant density or mildly compressible flows, with a predictor-corrector approach that couples the momentum and continuity equations. A collocated variable arrangement with a Rhie-Chow scheme for pressure-velocity coupling is implemented in a

SIMPLE-type algorithm (Siemens, 2022). In the canister-scale models, the Reynolds is low enough such that laminar flow is assumed. The momentum equation is then given by

$$\frac{\partial(\rho \mathbf{v})}{\partial t} + \nabla \cdot (\rho \mathbf{v} \otimes \mathbf{v}) = -\nabla \cdot (p\mathbf{I}) + \nabla \cdot \mathbf{T} + \mathbf{f}_b \tag{1}$$

Where $\mathbf{v}$ is the velocity vector, $\mathbf{T}$, is the stress tensor, and ρ is the density. The $\boldsymbol{f}_b$ term is the body force, solely occurring due to the buoyancy driven flow in this case. The viscous stress tensor is

$$\mathbf{T} = \mu(\nabla \mathbf{v} + (\nabla \mathbf{v})^T) - \frac{2}{3}\mu(\nabla \cdot \mathbf{v})\mathbf{I} \tag{2}$$

Where μ is the air viscosity. The mass conservation is expressed through the continuity equation

$$\frac{\partial \rho}{\partial t} + \nabla \cdot (\rho \mathbf{v}) = 0 \tag{3}$$

The conservation of energy gives an equation in terms of the total energy, E, as

$$\frac{\partial(\rho E)}{\partial t} + \nabla \cdot (\rho E \mathbf{v}) = \mathbf{f}_b \cdot \mathbf{v} + \nabla \cdot (\mathbf{v} \cdot \boldsymbol{\sigma}) - \nabla \cdot q + S_E \tag{4}$$

Where in the solid phases, the terms with $\mathbf{v}$ are equal to 0, q is the conductive heat flux, the energy source term S_E is due to the chemical reactions in the fluid phase and is from the specified heat source for the fuel plates in that solid region. The implicit solver in Star-CCM+ can typically adapt up to a Courant-Friedrichs-Lewy (CFL) condition of nearly 50. The properties for the materials used for each of the solid regions are shown in Table 1, it is assumed maximum temperatures are low enough to use constant thermal properties for solids.

Table 1. Physical properties of the components for a One-third scale DOE Standard Sealed canister.

Material	Density [kg/m^3]	Thermal Conductivity [W/m K]	Heat Capacity [J/kg K]	Emissivity [-]
Al-6061 (siding/back plates) (Polkinghorne, 1991)	2702	167	896	0.82
Stainless Steel 304 (Incropera et al. 2007)	7900	14.9	477	0.46
Stainless Steel 316 (Incropera et al. 2007)	8238	13.4	468	0.46
ATR Fuel Plates (Ilum 1996)	3680	42.6	614	0.82 (assumed)

2.2 Model Geometry

A design for an instrumented one-third scale canister design was created by SRNL (Herman et al., 2021). The schematic of the instrumented lid canister design is shown in Figure 1. The system is composed of a DSC fuel basket, a lid assembly (ported lid and mating top hat), and an instrument manifold to accommodate gas-sample sensors and thermocouples. The Instrumented Lid assembly has been designed, fabricated, and tested to be used as an apparatus for proposed long term (~10+ years) monitoring. The canister contains one Type-1a basket loaded with 10 ATR fuel elements. The dimensions for the Type1a basket are described in DOE/SNR/REP-90 with modifications for tolerance in DOE/REP/DSN-19. In the model, the outer canister is assumed to be stainless steel 316, and the inner basket stainless steel 304, the same materials in the DOE sealed standard canister. The green tubes in the diagram are for gas sampling lines and the yellow are for thermowells. The thermowells are set up with a measurement every 10 inches. Gas samples can be measured with a gas chromatograph with detection limits of about 100 ppm H_2 in helium, as well as 50 ppm for N_2 and O_2 (Herman et al., 2021).

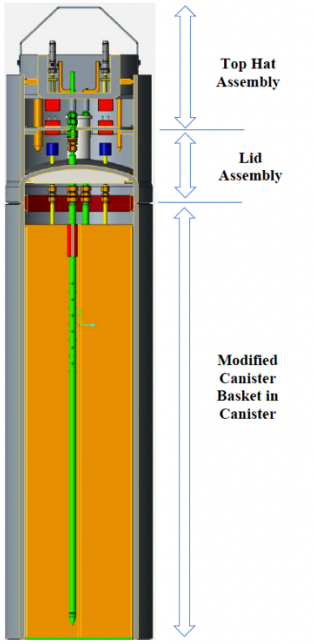

Figure 1. Design of the instrumented lid one-third scale canister (Herman et al., 2021).

The CAD model that was constructed and used for the simulations is shown Figure 2a. This represents the outer canister and its instrumented lid with the single Type 1a basket loaded with ATR fuel. The green lines show the approximate locations of the thermowells from the instrumented lid. The CAD for the ATR fuel is shown in Figure 2b, and the CAD for the Type 1a basket is shown in Figure 2c. Figure 2d shows a horizontal slice of the meshed domain used in the CFD simulations. The red denotes the fuel plates, the blue denotes the free volume of air, the light grey shows the aluminum side plates, the orange shows the basket, and the white shows the canister.

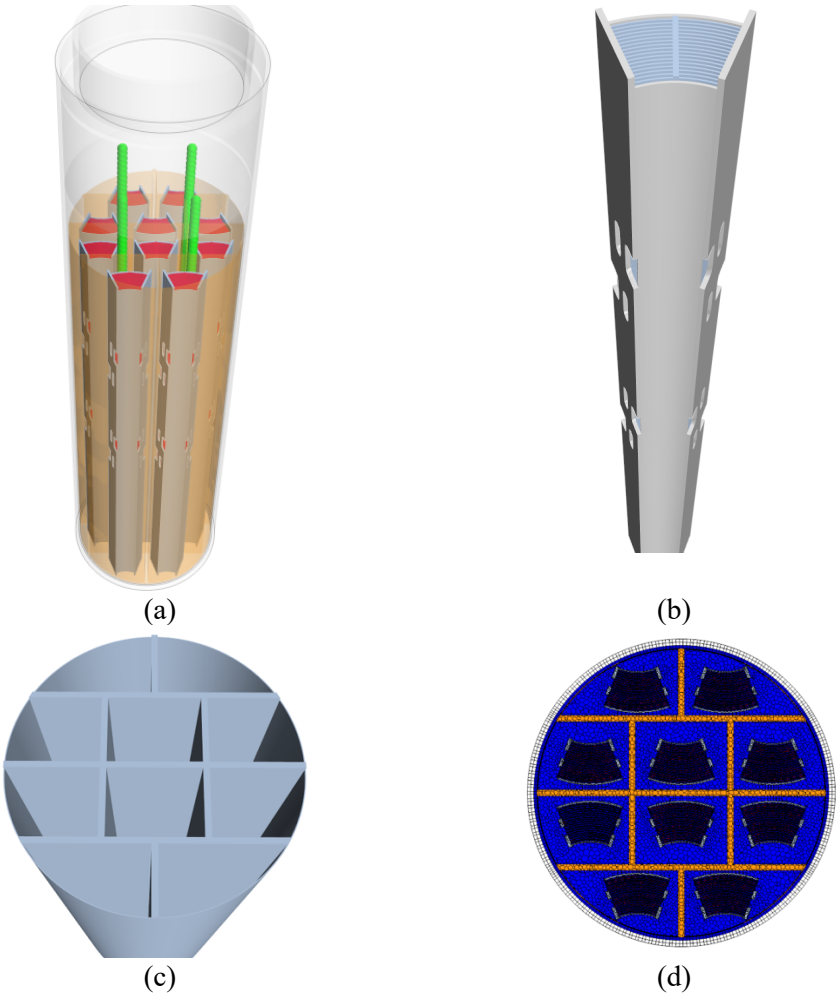

Figure 2. Domain used in simulations showing (a) fully loaded one-third scale canister, the CAD model for (b) ATR fuel element, and (c) Type-1a basket, and (d) horizontal mesh slice of the basket.

2.3 Sensitivity and Ambient Conditions

As with the prior studies, an assumption is made that exterior yearly temperatures for a 50-year storage scenario would mimic the conditions seen in the IFSF facility (Abboud and Huang, 2019b). Ambient temperatures for the INL INTEC CPP-603 facility are described in Christensen (2003a, b). A plot of the ambient temperature conditions measured when the facility had working thermocouples in 2011 is shown in Figure 2a, with 9 thermocouples recording once an hour over a year long period. The data in Figure 2b shows weeklong averages for comparison. The ambient temperature within the facility itself has a very small variation within it when compared to the exterior climate due to the large amount of mass of spent fuel stored within it. The largest temperature difference in a 12-hour span is only 1.5° C, and largest temperature difference in a week-long span is 4.4° C. This justifies the large timesteps used for the CFD model for the thermal history. Table 2 includes the parameter ranges used in the study for residual water, oxide thickness and dried/undried fuel cases. While drying is planned such that a completely undried case shouldn't occur, the undried fuel represents a worst case scenario for the incomplete drying of the fuel. Film oxyhydroxide layer thickness for a similar ASNF, from the University of Missouri research reactor (MURR) stored over a long duration in wet storage, were measured to be 5-10 μm (Olson et al., 2019). The boehmite film on the ATR fuel is specified to be 2-6 μm by the manufacturer before reactor operation, and 1-4 μm was observed on measurements of end box samples in

dry storage (Winston et al., 2020). To be on the conservative side, the full range of 1-10 μm was considered in the sensitivity analysis. A previous analysis of the fuel inventory list from Mortensen, 2016 to be moved into IFSF resulted in an average decay heat of 18 watts, with a standard deviation 12 watts. One standard deviation below was set as the lower bounds, and two standard deviations above was set as the upper bounds due to the large tail end of the distribution.

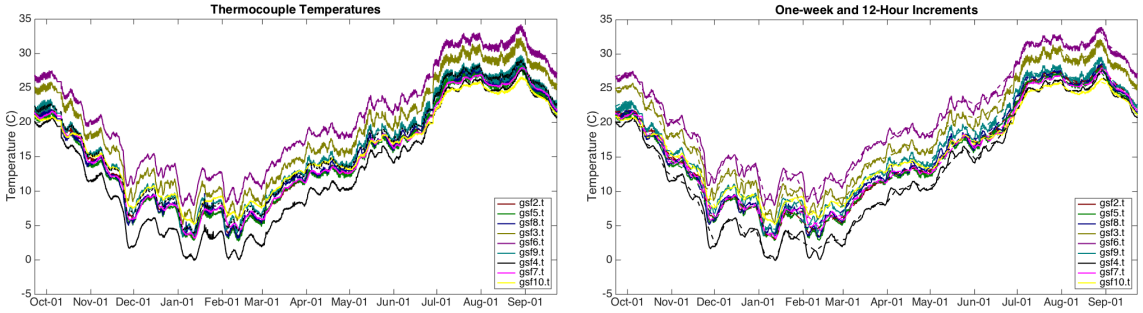

(a) (b)

Figure 2. Thermocouple measurements over 1 year in the INL CPP-603 facility for (a) one-hour intervals, (b) 12-hour and weekly intervals.

Table 2. Sensitivity parameters for this study.

Parameter	Lower Bound	Base Case	Upper Bound
Chemi-/Physio- sorbed water on ATR		1.01:1 H_2O to Al_2O_3	2.5:1 H_2O to Al_2O_3
Corrosion Layer Thickness [μm]	1	5	10
Decay Heat [W]	6	18	42

In ECAR 2906, MicroShield 9.01 was used to calculate the on-contact and 1-meter dosage rates for ATR fuel assemblies (Stewart 2012). Based on the decay heat for a given fuel assembly, the on-contact dosage rate can be estimated as

$$\dot{d} = 3.78 \times 10^{-3} Q, \tag{5}$$

in units of Gy/s, with Q as the decay heat rate given in Watts by

$$Q = Q_0 \exp\left(-0.023\, t_{year}\right) = Q_0 \exp(-7.2883 \times 10^{-10}\, t_{sec}\,) \tag{6}$$

2.4 Gas-Phase Chemical Equations

The chemical reactions which are considered are one-step reactions. The full chemical reaction mechanism from Wittman & Hanson, 2015, is utilized. This full mechanism contains 40 chemical species and 115 total reactions. This model was developed from literature for a full set of chemical reactions using prior experimental collection of radiolysis data (Bulearca et al., 2010, Atkinson et al., 2004; Arkhipov et al., 2007), and was used in the latest model of the DOE sealed standard canister with surface chemistry (Abboud 2022). Due to the nature of the time period interest of this study, it would be infeasible to fully resolve all 40 chemical species and 115 total reactions within the canister due to the computational cost of multiphysics CFD models. The model utilizes Cantera for solution of the chemical reactions. The source term of chemical species is

$$\frac{d[A_i]}{dt} = \dot{d}\sum G_i w_g[A_g] + \sum k_{ir}\prod[A_{jr}]^{O_{jr}} \tag{7}$$

Where $\dot{d}$ is the dose rate, G_i is the G-value for the radiolytic decomposition, w_g is the molecular weight, k_{ir} is the reaction rate, and O_{jr} is the reaction order for species j. The transport equations for the species mass fractions, Y_i, are solved for N-1 species as

$$\frac{\partial \rho Y_i}{\partial t} + \nabla \cdot (\rho v Y_i) = \nabla \cdot \left(J_i + \frac{\mu_t}{\sigma_t}\nabla Y_i\right) + S_{Y_i} \tag{8}$$

The source term here, S_{Y_i}, is reformulated from equation 7 to be in terms of the mass fractions rather than concentration. The basic diffusion is defined as

$$J_i = \rho D_{i,m} \nabla Y_i \tag{9}$$

Where $D_{i,m}$ is the binary diffusion coefficient. The general reaction term is defined as

$$k_{ir} = k_{ir}^0 T^{x_r} \exp\left(-\frac{E_a}{RT}\right) \tag{10}$$

2.5 Surface Chemistry

Based on the work completed by associated tasks in the ongoing investigations into storage of aluminum-clad spent nuclear fuel, the surface chemistry associated with the aluminum cladding was added into the model to be coupled with the Wittman and Hanson gas phase model. This is done through work outlined for the radiolytic yield of the aluminum hydroxide (Zalupski 2018), the general surface corrosion (Lister 2018), and prior kinetic expressions for aluminum corrosion. The surface chemistry built in Cantera is intended for catalytic reactions, though it is utilized here, it allows for all parts of the metal to be reactive even if not at the surface. However, since this estimate is a conservative approximation, it should provide an upper bound. In creating the surface, first the number of moles of AlOOH present is calculated based on the plate thickness, and surface area of the plates

$$n_{AlOOH} = \frac{A_{fuel} th_{AlOOH} \rho_{AlOOH}}{MW_{AlOOH}} \tag{11}$$

And the ratio of moles of oxide to moles of aluminum alloy is assumed proportional to the film thickness and the plate thickness

$$\theta_{AlOOH} = \frac{th_{AlOOH}}{th_{plate}/2} \tag{12}$$

While this may underestimate total aluminum present to have a single surface, it is not that reactive at low temperatures. The calculation of the site density with this assumption is then

$$\rho_s = \frac{n_{AlOOH}}{X_{AlOOH} A_{fuel}} \tag{13}$$

The moles present for reaction is then

$$[\mathrm{AlOOH}] = \theta_{AlOOH}\rho_s \tag{14}$$

With this formulation of the surface sites, the following reaction is implemented for radiolysis of boehmite film

$$2\ \mathrm{AlOOH(S)} \xrightarrow{\gamma} 2\ \mathrm{AlOO(S)} + 2\ \mathrm{H}\cdot \tag{15}$$

With the hydrogen radical determined through a combination of model tuning, and atomistic theory (Westbrook et al. 2015). The G-value used here was updated from the previous work to be specific to a helium back-filled environment, and be dependent on the total sample mass inside of the corrosion layer mass. This effectively changes the reaction from 1st order with regards to the corrosion layer to 0th order. For the undried fuel cases a G-value of 4.91×10^{-10} mol/J, and for the undried cases a G-value of 9.35×10^{-11} is used fit to data. In the model above a total dose of 2 MGy the G-value is switched to 2.0×10^{-10} mol/J for the undried case and 4.25×10^{-11} for the dried case to artificially produce the early- and late-stage hydrogen generation rates from the experiments. This chemistry likely needs to be revisited as future experimental data becomes available. Figure 3 shows the chemical model that was set up to replicate the mini-canister tests with this bi-linear fit for the G-value in comparison to the actual experimental data for the as-corroded plates in Figure 3a and the as-dried plates in Figure 3b.

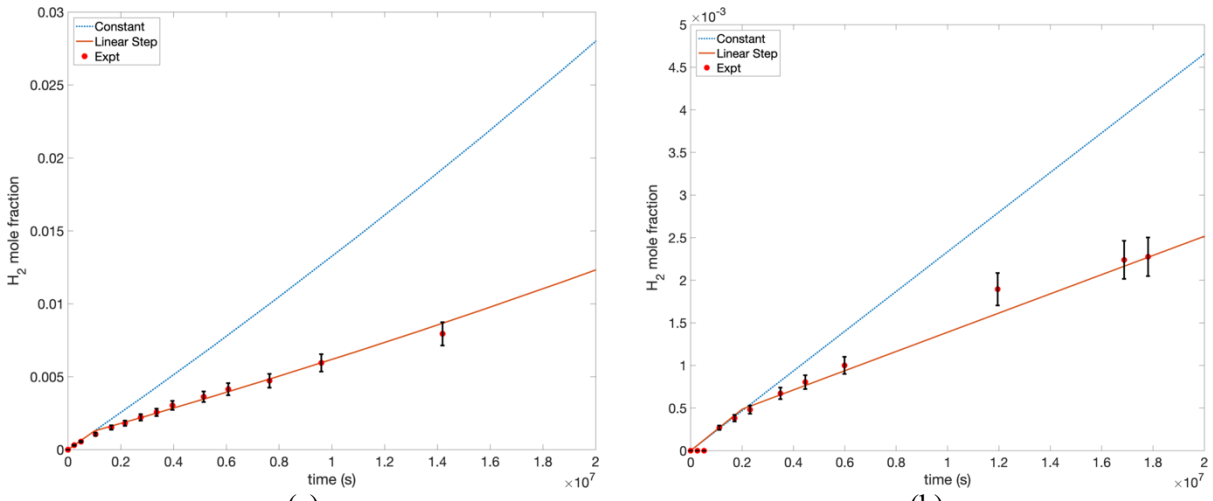

(a) (b)

Figure 3. Mini-canister model data fitted with the bi-linear chemical model for the (a) as-corroded and (b) as-dried surrogate plates. The blue line shows the reference for a constant G-value model.

Another reaction is included with a slow rate to convert the intermediate AlOO to stable Al_2O_3. The thermal dehydration of boehmite at low temperatures was also considered. The mass loss of aluminum oxyhydroxide coupons was considered to be from the loss of water in determining the kinetic rate according to the reaction

$$\mathrm{AlOOH}\cdot(1.5\ \mathrm{H_2O})(\mathrm{S}) \leftrightarrow 2\ \mathrm{ALOOH(S)} + 1.5\ \mathrm{H_2O(g)} \tag{16}$$

This reaction was fit to the mass loss of the coupons ranging from 25 to 180 °C (Lister and Orme 2019). For a conservative approximation on undried cases, the upper end of pseudo boehmite was assumed with a 2.5:1 H_2O to Al_2O_3 ratio (Vedder and Vermilyea 1969). Lastly, the general corrosion of aluminum in the event that the oxyhydroxide layer was consumed was also considered from an older study (Hilton, 2000). This reaction was adapted from aluminum in water rather than humid air, and so should be conservative to include the reaction of

$$Al(S) + 1.5\ H_2O \rightarrow 0.5\ Al_2O_3(S) + 1.5H_2(g) \quad (17)$$

Though it should be noted this last equation has the most minimal effect. At an average surface temperature of 50 °C, the total aluminum corrosion would only equation to 1.2 grams after 50 years, or 58 grams after 50 years at 200 °C surface temperature.

3. Results and Discussion

The model was simulated out to a time period of 50 years similar to the extended storage period previously modeled, though the lifetime of canister monitoring could be of a period of 10 years. The results also show a close-up of the first 2 years to indicate where initial validation of the model with gas sampling data is more likely to occur.

3.1 CFD Modeling

The method for modeling the CFD aspect of the one-third scale canister was the same as the previous full-scale model. The model was initialized with a steady state condition at the prescribed fuel decay heat, then pseudo-steady state conditions for the velocity were assumed to allow for large timesteps to be made to achieve a 50-year history of the temperature profile in the canister. The horizontal slice in the center of the canister for the temperature is shown in Figure 4a-c for the low to high decay heat at the initial condition. The corresponding vertical temperature distribution is shown in Figure 4d-f for low to high decay heat, with the temperature at vertical lines extrapolated at the approximate locations of the instrumented lid's thermowells shown in Figure 4g-i for low to high decay heat. There is more vertical variation in temperature as the decay heat is increased, and the head space above the fuel shows a large drop in the temperature and shows less-uniform profiles at higher decay heats with higher velocities and more unstructured recirculation that occur. The plot of the average gas temperature over a 50-year period is shown in Figure 4j for the three decay heats.

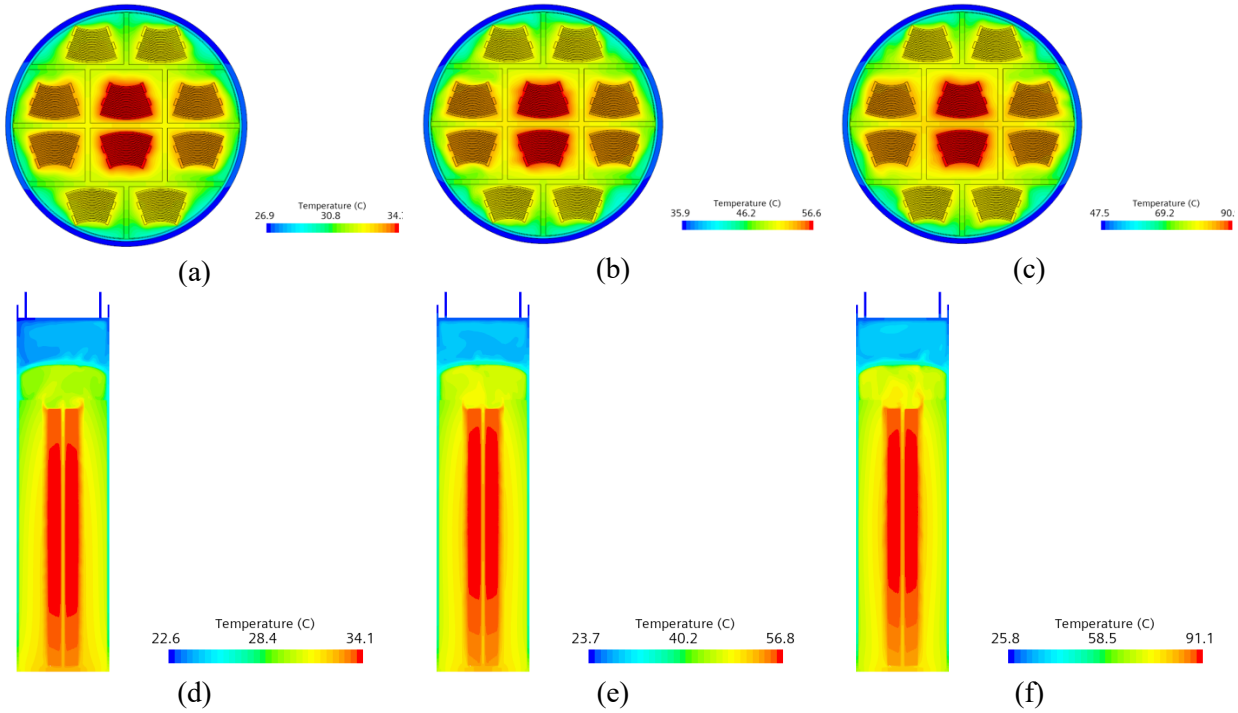

(a) (b) (c)

(d) (e) (f)

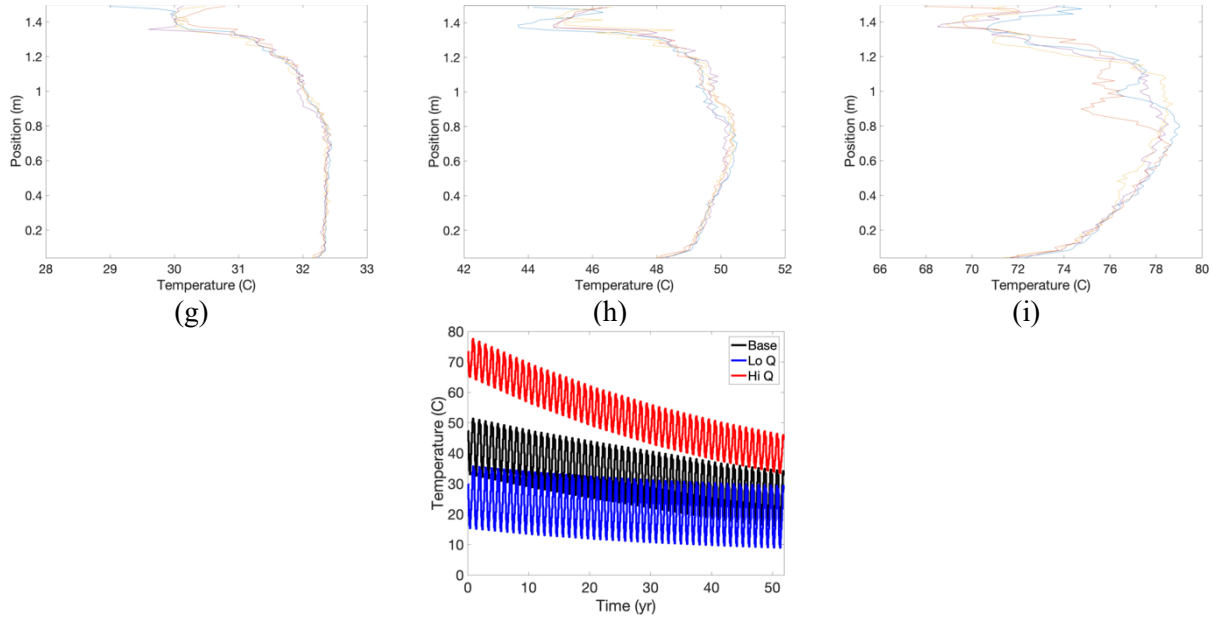

Figure 4. Horizontal temperature contour for the center of the basket in the canister for the initial conditions for the (a) lower, (b) nominal and (c) upper decay heat cases. Vertical temperature contour for the central basket in the canister for the initial conditions for the (d) lower, (e) nominal and (f) upper decay heat cases, with corresponding thermowell plots (g) lower, (h) nominal and (i) upper decay heat cases. The (j) 50-year average temperature profile (Legend: Q = decay heat).

The CFD profile of the velocity across the center of the basket is shown in Figure 5a-c for the lower to upper decay heat cases. The streamlines of the recirculation that occurs through the canister are shown in Figure 5d-f for the lower to upper decay heat cases in the canister. Flow directly around the fuel elements is minimal. Some upwards flow occurs from the center of the bucket and some downwards recirculation along the outer edge of the canister. There is a recirculation zone that also occurs in the head space above the basket. Maximum velocities are increased by a little over a factor of 2 from the low to high decay heat cases.

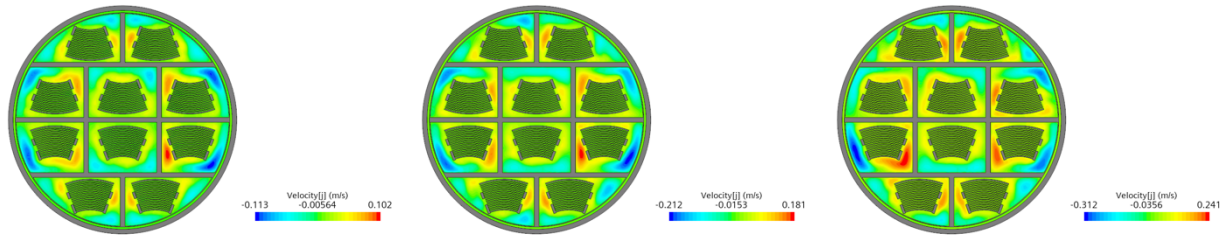

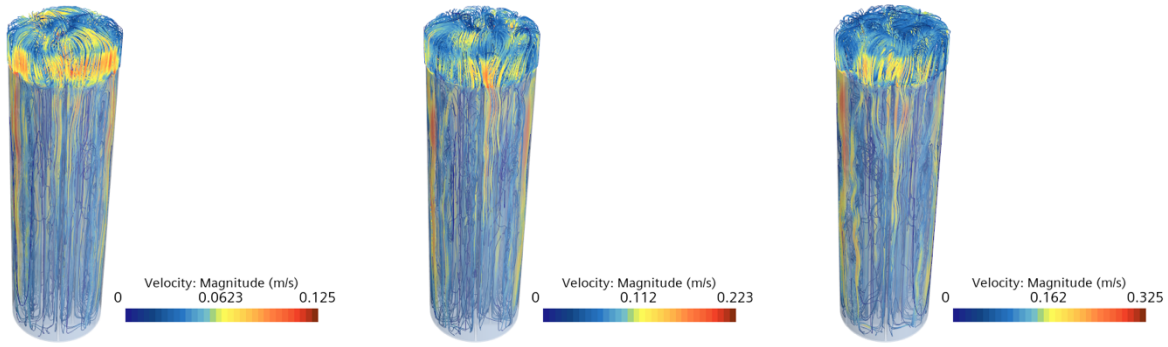

(d) (e) (f)

Figure 5. Horizontal velocity for the center of the basket in the canister for the initial conditions for the (a) lower, (b) nominal and (c) upper decay heat cases. Velocity streamlines in the the canister for the initial conditions for the (d) lower, (e) nominal and (f) upper decay heat cases.

3.2 Chemical Modeling – Dried Fuel

The chemical modeling for the one-third scale canister does not show any significant changes from the previously modeled systems. That is, the hydrogen concentration remains the primary species of interest, no oxygen formation is observed, and pressure remains well below canister limits. Figure 6 shows the hydrogen concentration for the modeled cases for fully dried fuel. This is split to show the 2-year, 10-year and 50-year time frame. The kink in hydrogen rates occurs due to the bi-linear function for the G-value. At the long time 50-year frame, this is less visible, but when examining the short year timeframe this effect is readily apparent in the model. The nominal case here results in only about 1% mole hydrogen after a 10-year span. Observations that can be made directly with the model over a short time-period show less than 0.3% by mole hydrogen in the first 2 years. The range in the predicted value is about 0.5% depending on the decay heat for the cases. No change in hydrogen generation as a function of corrosion layer thickness is seen for dried fuel. Based on the slope of the hydrogen generation, the rate of increase in on the order of 100 ppm/month, similar to the detection limits of the GC setup for the instrumented lid.

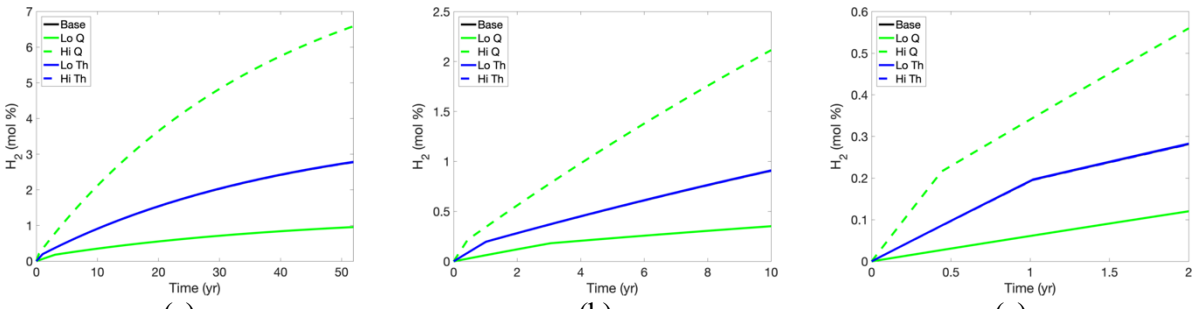

(a) (b) (c)

Figure 6. Hydrogen generation for dried fuel scenario for the (a) extended 50-year storage period, (b) 10-year monitoring, and (c) 2-year initial model validation. Legend: Q = decay heat, Th = oxyhydroxide thickness.

The results for the absolute pressure are shown in Figure 7 for the dried fuel cases. The pressure shows a minor buildup at first then decays as the overall temperature of the cases decreases. Fluctuations are on the order of 0.1 atm due ot external temperature changes. Then the pressure just oscillates as a function of the exterior temperature of the canister. The maximum absolute pressure is only 1.28 atm, well under any mechanical limits. The pressure shows only small effects from the varied parameters of fuel decay heat and corrosion layer thickness.

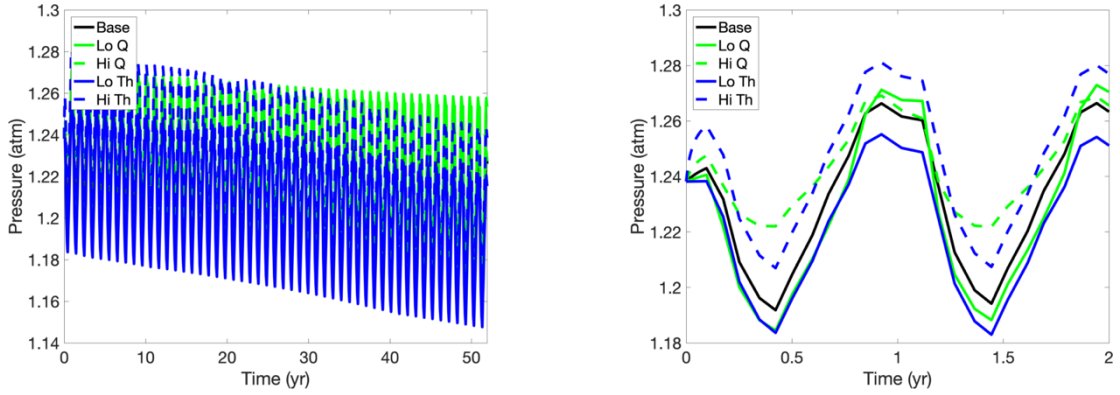

Figure 7. Pressure build-up for dried fuel scenario for the (a) 50-year extended storage and (b) first 2 years of storage. Legend: Q = decay heat, Th = oxyhydroxide thickness.

For the case with residual air, as with the case with pure helium, no significant changes are seen in the chemical species from prior modeling efforts. Nitric acid remains the main component that can possibly form with N_2 present. Figure 8 shows the hydrogen concentration for the modeled cases for fully dried fuel. This is split to show the 2-year, 10-year and 50-year time frame. The hydrogen present consumes oxygen to form additional water vapor, and until sufficient oxygen is consumed, the total hydrogen production is depressed during the early time-period of the model. While after 50 years this reaches nearly the same amount of hydrogen as in pure helium, in the first two years of the timespan the model shows depressed hydrogen less than 0.02% for most of the cases modeled. Due to the higher dose rate, the high decay heat case reaches this point faster.

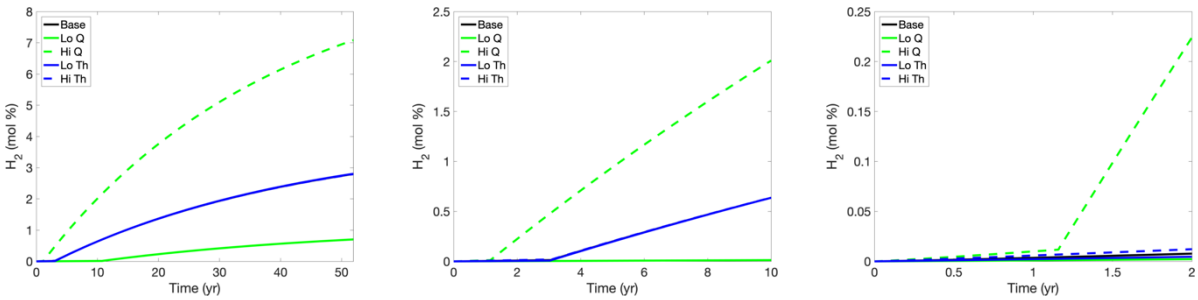

Figure 8. Hydrogen generation for dried fuel scenario with residual air for the (a) 50-year extended storage period, (b) 10-year monitoring, and (c) 2-year initial model validation. Legend: Q = decay heat, Th = oxyhydroxide thickness.

The results for the nitric acid for the cases with residual air present are shown in Figure 9, split into the 50-year, 10-year and 2-year time spans. The nitric acid generation rate is nearly constant over the initial several years of the model and does not roll over and decrease until near the full 50-year timeframe.

The nitric acid generation is rather small over the first two years only reaching about 100 ppm. The main variation occurs with the decay heat of the fuel, the corrosion layer thickness has a negligible effect. This variation is about 200 ppm over the 2-year time span, but increases to 3000 ppm over a 50 year long period. No changes are seen as a function of the corrosion layer thickness.

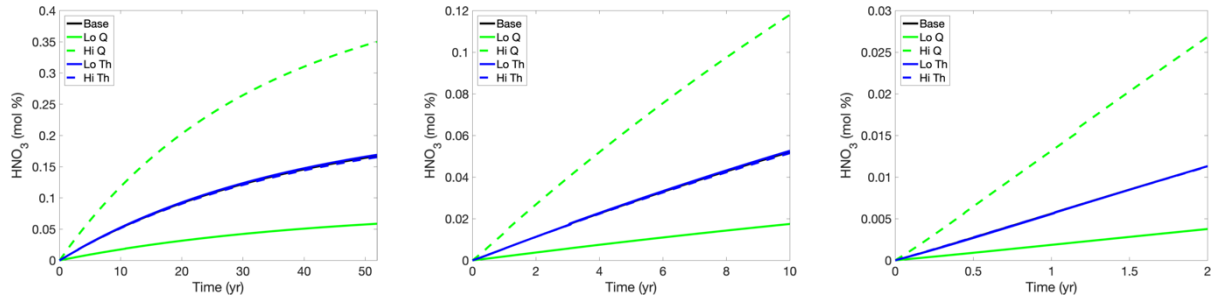

(a) (b) (c)

Figure 9. Nitric acid generation for dried fuel scenario with residual air for the (a) 50-year extended storage period, (b) 10-year monitoring, and (c) 2-year initial model validation. Legend: Q = decay heat, Th = oxyhydroxide thickness.

The results for the pressure are shown in Figure 10 for the cases with residual air present. Nearly no difference is seen in the pressure under this scenario from the cases with pure helium. This shows a decrease over time after the initial period, followed by oscillations dependent on the external temperature of the canister. Pressure variation as a function of the corrosion layer thickness and fuel decay heat is minimal.

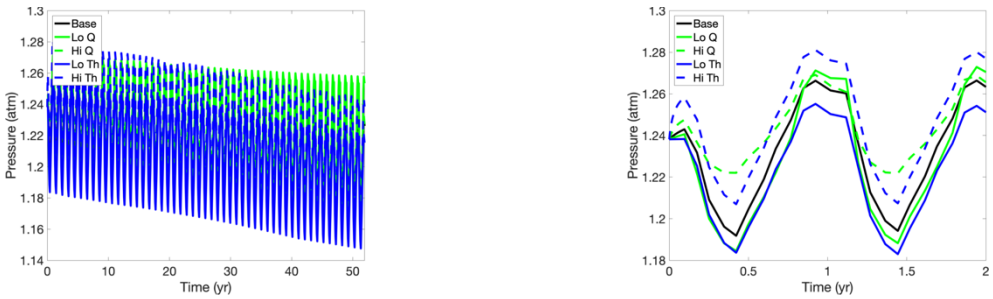

(a) (b)

Figure 10. Pressure build-up for dried fuel scenario with residual air for the (a) 50-year extended storage and (b) first two years of storage. Legend: Q = decay heat, Th = oxyhydroxide thickness.

As noted, in the presence of air, within the first few months of the simulated time period, there is a delay in the hydrogen generation rates. This effect is not new in the chemical model, but is obfuscated in long-term results, as it has little effect on the 50-year chemical composition. This occurs as the residual O_2 is consumed by H radical to form additional water vapor. Once most of the O_2 is consumed in this way hydrogen is generated at the same rate as in the cases with pure helium. The concentrations of oxygen, water vapor, and hydrogen is shown for the base model with residual air in Figure 11 to show the effect more closely.

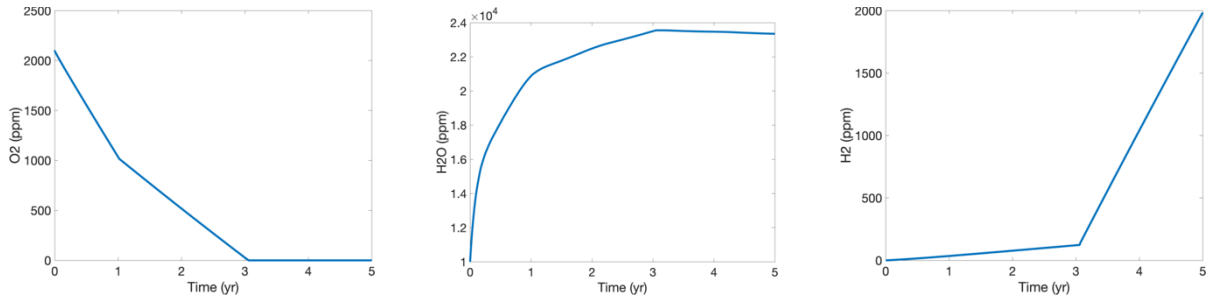

(a) (b) (c)

Figure 11. The (a) oxygen, (b) water vapor and (c) hydrogen concentration for the nominal case with residual air scenario.

The summary of the hydrogen concentration, maximum canister pressure, and nitric acid concentration in the presence of air is shown in Table 3. The results are tabulated for the 1-year, 10-year and full 50-year time-period. Of note, every case will not exceed the 4% lower flammability limit during a 10-year storage demonstration. Only the high decay heat case will exceed this limit during a 50-year storage period.

Table 3. Results for a sealed canister for dried fuel.

	Pure Helium		Helium + 1% air		
Case / Variable Max	Pressure (atm)	H_2 (%) 1/10/50 yr	Pressure (atm)	H_2 (%) 1/10/50 yr	HNO_3 (ppm) 1/10/50 yr
Base (18W, 5µm thickness)	1.26	0.19/0.91/ 2.78	1.27	0.003/0.64/2.80	56/521/1672
Low decay heat (6W)	1.26	0.06/0.35/ 0.96	1.27	0.0009/0.012- 0.70	19/174/586
High decay heat (42W)	1.27	0.34/2.11/ 6.58	1.27	0.01/2.01/7.08	131/1179/3500
Low Thickness (1 µm)	1.25	0.19/0.91/ 2.78	1.26	0.002/0.64/2.8	55/526/1690
High Thickness (10 µm)	1.28	0.19/0.91/ 2.77	1.28	0.006/0.64/2.8	56/515/1652

3.3 Chemical Modeling – Undried Fuel

As with the dried fuel case, the chemical modeling for undried fuel for the one-third scale canister does not show any significant changes from the previously modeled systems. That is, the hydrogen concentration remains the primary species of interest, no oxygen formation is observed, and pressure remains well below canister limits. Figure 12 shows the hydrogen concentration for the modeled cases for

undried fuel. This is split to show the 2-year, 10-year and 50-year time frame. The nominal case here results in only about 2% mole hydrogen after a 10-year span. Observations that can be made directly with the model over a short 2-year time-period show less than 1% by mole hydrogen. The range in prediction is about 1.3% depending on the decay heat for the cases. With undried fuel there is some variation in the hydrogen concentration based on the corrosion layer thickness of about 0.4% over the first two years due to the amount of water that is present.

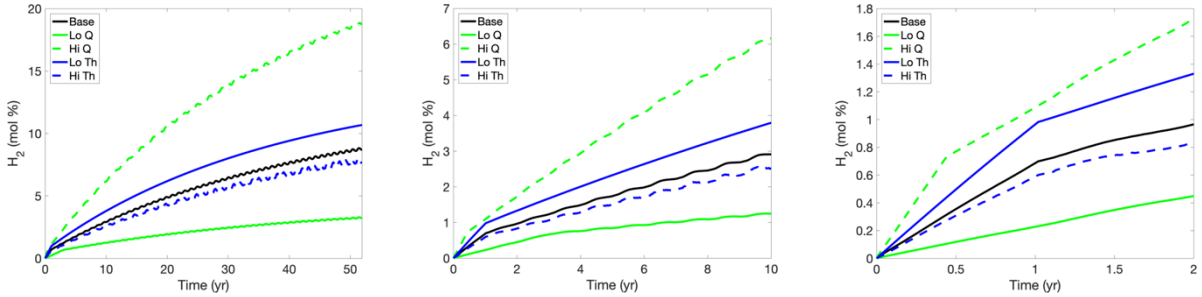

(a) (b) (c)

Figure 12. Hydrogen generation for undried fuel scenario for the (a) 50-year extended storage, (b) 10-year storage and (c) 2-year storage for undried fuel. Legend: Q = decay heat, Th = oxyhydroxide thickness.

The results for the pressure for the undried fuel are shown in Figure 13 for the cases. For undried fuel the pressure change is much higher as water vapor is released form the surface at higher temperatures. The decay heat of the fuel and the corrosion layer thickness have about the same effect on pressure at long time periods. The corrosion layer thickness has the largest variation as changes in pressure are minimal if the corrosion layer layer is small enough. For the pressure spike, most of the gain occurs over the initial few months of the simulation as it starts with the highest temperatures. The nominal case reaches about 1.8 atm, and the maximum absolute pressure that is reached across all scenarios is about 2.2 atm.

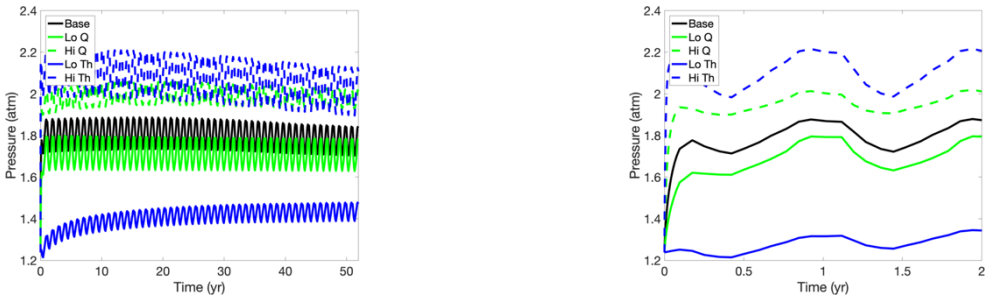

(a) (b)

Figure 13. Pressure build-up for undried fuel scenario for the (a) 50-year extended storage and (b) first 2 years of storage for undried fuel. Legend: Q = decay heat, Th = oxyhydroxide thickness.

For the case with residual air, as with the case with pure helium, no significant changes in chemical composition are seen in the chemical species from the previous modeling. Nitric acid remains the main component that can possibly form with N_2 present. Figure 14 shows the hydrogen concentration for the modeled cases for undried fuel. This is split to show the 2-year, 10-year and 50-year time frame. The overall hydrogen generation at long timeframes is essentially the same. However, at short time spans the effects mentioned before with the consumption of oxygen prevent significant hydrogen build up for the initial modeling period. This lowers the nominal hydrogen concentration after 2-years to 0.6%. The

additional water vapor present, and the higher G-value used for undried fuel result in much higher total hydrogen concentrations than the undried fuel cases.

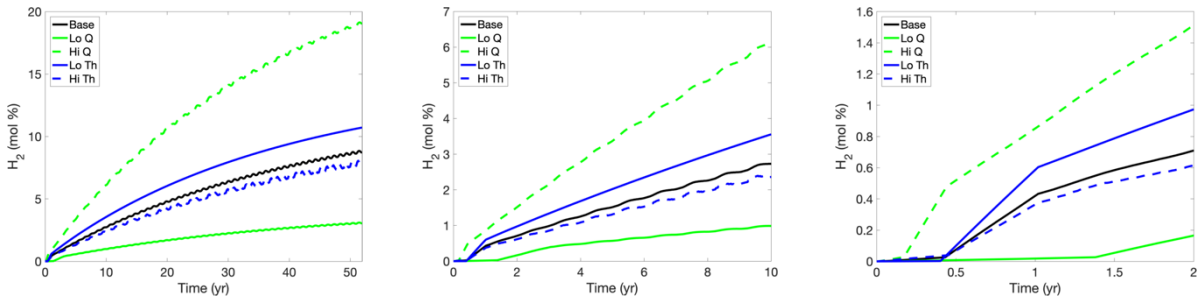

Figure 14. Hydrogen generation for undried fuel scenario with residual air for the (a) 50-year extended storage, (b) 10-year storage and (c) 2-year storage for undried fuel with residual air. Legend: Q = decay heat, Th = oxyhydroxide thickness.

The nitric acid for the undried fuel case with residual air is shown in Figure 15 for the time periods of 50, 10 and 2 years. With the undried fuel case, the potential nitic acid concentrations are lower than in the dried case due to the increased amount of water vapor in the gas, but the total moles remain about the same. The mole percentage is less than 0.01% after the first year of the model and increases to right around 0.1% by the 50-year timeframe. The decay heat affects the nitric acid generation the most, with a maximum of 0.2%. There is some small variation of the nitric acid concentration with the corrosion layer thickness.

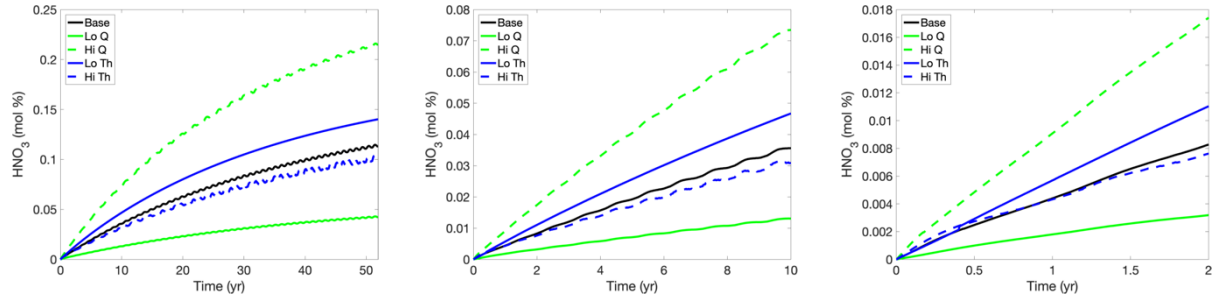

Figure 15. Nitric acid generation for undried fuel scenario with residual air for the (a) 50-year extended storage, (b) 10-year storage and (c) 2-year storage for undried fuel with residual air. Legend: Q = decay heat, Th = oxyhydroxide thickness.

The results for the pressure are shown in Figure 16 for the cases with residual air for undried fuel. The pressure is nearly unchanged from the case with pure helium shown in Figure 12. The maximum pressure across the cases remains about 2.2 atm with high corrosion layer thickness, and the nominal case is about 1.8 atm. The pressure decays slowly over time as the canister temperature decreases.

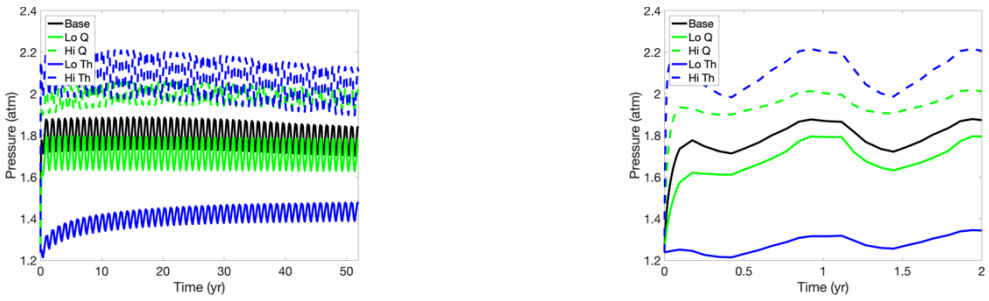

Figure 16. Pressure build-up for undried fuel scenario for the (a) 50-year extended storage and (b) first two years of storage for residual air case with undried fuel. Legend: Q = decay heat, Th = oxyhydroxide thickness.

The summary of the hydrogen concentration, maximum canister pressure, and nitric acid generation in the presence of air is shown in Table 4 for the undried fuel. The results are tabulated for the 1-year, 10-year and full 50-year time-period. For a 10-year monitoring period, only the scenario with high decay heat will reach the 4% lower flammability limit. However, for all cases except at low decay heat, this level will eventually be exceeded in a 50-year timespan for the undried fuel.

Table 4. Results for a sealed canister for undried fuel.

	Pure Helium		Helium + 1% air		
Case / Variable Max	Pressure (atm)	H_2 (%) 1/10/50 yr	Pressure (atm)	H_2 (%) 1/10/50 yr	HNO_3 (ppm) 1/10/50 yr
Base (18W, 5µm thickness)	1.89	0.69/2.91/ 8.82	1.89	0.42/2.73/8.85	44/356/1147
Low decay heat (6W)	1.80	0.23/1.25/ 3.29	1.80	0.018/0.99/3.10	18/131/430
High decay heat (42W)	2.06	1.09/6.16/ 18.8	2.06	0.85/6.10/19.1	91/735/2160
Low Thickness (1 µm)	1.48	0.96/2.78/ 10.7	1.48	0.59/3.56/10.72	57/467/1402
High Thickness (10 µm)	2.22	0.59/2.56/ 8.04	2.22	0.36/2.39/8.06	43/313/1037

4. Conclusions

A CFD-chemical model was created for a one-third scale instrumented lid canister. This canister is designed as a monitored demonstration of a full-scale DOE sealed standard canister. The results of the chemical model can be compared with data collected from the instrumented lid canister when that demonstration is underway, and validation of the results will provide confidence to the outcome of the model over the full predictive time span for the full-scale DOE sealed standard canister.

For dried fuel of the nominal decay heat (18W), the predicted hydrogen concentration is 0.19% after 1 year, 0.91% after 10 years, and 2.8% after 50 years, with a maximum pressure of 1.26 atm. Consistent with previous modeling, the decay heat of the fuel is the main factor that influences the results. For dried fuel in pure helium the hydrogen concentration ranges from 0.06% to 0.34% after 1 year, 0.35-2.11% after 10 years and 0.95 to 6.6% after 50 years. Due to the higher G-value measured experimentally, undried fuel exhibits much higher hydrogen generation rates. For undried fuel in pure helium, the hydrogen concentration ranges from 0.23 to 1.2% after 1 year, 1.25-6.2% after 10 years and 8.8 to 18.84% after 50 years. While long-term results for hydrogen concentration in the presence of residual air are mostly the same, early reactions with O_2 can delay significant production of H_2 until it is consumed to by forming more water vapor, lowering the range to 0.001 to 0.01% after 1 year. The maximum absolute pressure that is reached across any scenario is 2.06 atm, far below any mechanical limits for a canister. In the event of residual air, the presence of nitric acid is possible in the range of 18-131 ppm after 1 year, 174-1180 ppm after 10 years, and 586-3500 ppm after 50 years. If the fuel is sufficiently dried, or of nominal decay heat (<18W), the 4% lower flammability limit of hydrogen will not be reached within a 10-year monitoring period.

Some of the next steps for this model are to consider DOE standard canister cases which are more densely packed, thereby reducing the free volume available for gas evolution, which may result in higher hydrogen concentrations and pressures within the canisters. In addition, as experimental data is collected by experimental tasks, the surface chemistry reactions used within the model may be adjusted. The design is being planned for a demonstration case for the HFIR fuel elements, and this model can be used to provide predictive results for that scenario.

REFERENCES

Abboud, A.W. and Huang, H., 2018. Transient Coupled Chemical-Thermal-Fluid Field Simulation of Sealed Aluminum-clad Spent Nuclear Fuel Storage Canister, Tech. rep. INL/EXT-18-51683.

Abboud, A.W. and Huang, H., 2019. Sensitivity Study of Coupled Chemical-CFD Simulations for Sealed and Unsealed Aluminum-clad Spent Nuclear Fuel Storage Canisters. Idaho National Laboratory, Tech. rep. INL/EXT-19-52650.

Abboud, A.W., 2021. Modeling Summary of ASNF in DOE Sealed Standard Canisters, Idaho National Laboratory, Tech. rep. INL/EXT-21-64413.

Abboud, A.W. 2022. Modeling of Radiolytic Hydrogen Generation of Irradiated Surrogate Aluminum Plates. Idaho National Laboratory, Tech rep. INL/RPT-22-66504.

Abboud, A. W. 2022. Sensitivity study of coupled chemical-CFD simulations for analyzing aluminum-clad spent nuclear fuel storage in sealed canisters. Nuclear Engineering and Design, 390, 111691.

Arkhipov, O.P., Verkhovskaya, A.O., Kabakchi, S.A., and Ermakov, A.N., 2007. Development and verification of a mathematical model of the radiolysis of water vapor. Atomic Energy, 103(5):870.

Atkinson, R., Baulch, D.L., Cox, R.A., Crowley, J.N., Hampson, R.F., Hynes, R.G., Jenkin, M.E., Rossie, M.J., and Troe, J., 2004. Evaluated kinetic and photochemical data for atmospheric chemistry: volume I – gas phase reactions of X, HOx, NO2, and SOx species. Atmospheric Chemistry and Physics, 4(6): 1461-1738.

Bulearca, A.M., Calinescu, I., and Lavric, V., 2010. Model Studies of NOx and SOx reactions in Flue gas treatment by electron beam. UPB Sci Bull, Series B, 72(1):101-112.

Christensen, A., 2003a. EDF-2760, The Irradiated Fuel Storage Facility Maximum Heat Load And Resulting Maximum Temperatures When the Ventilation System Is Not Operating. Tech. rep., Idaho National Laboratory.

Christensen, A., 2003b. EDF-5579 Corrosion Potential of the Irradiated Fuel Storage Facility Environment. Tech. rep., Idaho National Laboratory.

Goodwin, D.G., Moffat, H.K., and Speth, R.L. *Cantera: An object-oriented software toolkit for chemical kinetics, thermodynamics, and transport processes*. http://www.cantera.org, 2017. Version 2.3.0. doi:10.5281/zenodo.170284

Herman, D.T., McNamara, J.D., Randall, B.C., McNight, A.S., Verst, C.G., d'Entremont, A., Pak, D.J., Duncan, A.J., Sindelar, R.L., Abboud A.W., Jarrell, J.J., and Connolly, M.J. Instrumented Lid for Monitoring SNF in Dry Storage. 2021. Waste Management 2021 Conference, March 8-12, 2021, Phoenix, AZ, USA.

Hilton, B.A. 2000. Review of Oxidation Rates of DOE Spent Nuclear Fuel Part 1: Metallic Fuel. Tech. rep. Argonne National Laboratory, AN-00/24.

Horne, G.P., Conrad, J.K., Copeland-Johnson, T.M., Pu, X., Khanolkar, A., Wilbanks, J.R. and Pilgrim, C.D. 2022. Milestone 1.2.10: Steady-state H2 roll-over point data for aluminum alloys 1100 and 6061. INL-RPT-22-68379. Tech. Rep. Idaho National Laboratory.

Illum, D.B., 1996. ATR Fuel Summary Report. Tech. Report INEL-96/300.

Incropera F.P., DeWitt, D.P., Bergman, T.L. and Lavine, A.S., 2007. Fundamentals of Heat and Mass Transfer, Sixth Edition, John Wiley and Sons, Hoboken, NJ.

Kim, S. S., Pope, C. and Taylor, L. L. 2007. Criticality analysis for proposed maximum fuel loading in a standardized snf canister with type 1a baskets, INL/EXT-07-12326. Tech. rep., Idaho National Laboratory.

Lister, T. 2018. Vapor Phase Corrosion Testing of Pretreated AA1100. Tech. Rep. Idaho National Laboratory, INL/EXT-18-52249.

Lister, T and Orme, C. 2019. Analysis of Vapor Phase Corrosion of Pretreated Aluminum Alloys. Tech. Rep. Idaho National Laboratory, INL/EXT-19-55558.

Mortensen, K., 2016, EDF-10891, Decay Heat of ATR Elements to be Transferred from CPP-666 FSA to IFSF, Tech. rep., Idaho National Laboratory.

Olson, L., Verst, C., d'Entremont, A., Fuentes, R., and Sindelar, R. 2019. Characterization of Oxide Films on Aluminum Materials following Reactor Exposure and Wet Storage in the SRS L-Basin. Tech. Rep. Savannah River National Laboratory, SRNL-STI-2019-00058.

Parker-Quaife E.H., Horne, G.P., Heathman, C.R., Verst, C., and Zalupski, P.R. 2019. Radiation-Induced Molecular Hydrogen Gas Generation by Pre-Corroded Aluminum Alloy 1100. Tech Rep. Idaho National Laboratory, INL/EXT-19-55202.

Parker-Quaife E.H. and Horne, G.P. 2021. Milestone 2.8: Preliminary Radiolytic Gas Generation Measurements from Helium-Backfilled Samples. Tech. Rep. Idaho National Laboratory, INL/EXT-21-61404.

Polkinghorne, S.T. and Lacy, J.M. 1991. Thermophysical and Mechanical Properties of ATR Core Materials, Report No. PG-T-91-031, EG&G Idaho Inc.

Siemens, 2022. User Guide: Star-ccm+ v17.04.008R8.

Snow, S.D. 2008. Design Considerations for the Standardized DOE SNF Canister Internals, Tech. Rep., U.S. Department of Energy, DOE/SNF/DSN-19.

Stewart, D. 2012, ECAR-2906. ATR Fuel Element In-Air Dose Rate Estimates Base on Heat Generation, Tech rep., Idaho National Laboratory.

Taylor, L.L. 2004. Packaging Strategies for Criticality Safety for “Other” DOE Fuels in a Repository, Tech. Rep., U.S. Department of Energy, DOE/SNF/REP-090.

Vedder, W. and Vermilyea, D.A. 1968. Aluminum + Water Reaction. Trans. Faraday Soc, 65, pp.5 61-584.

Verst, C.G. and d’Entremont A.L. Measurement of Radiolytic Hydrogen Generation and Impact of Drying Treatments on Reactor-Exposed and Surrogate Aluminum Materials. Tech. rep. Savannah River National Laboratory, November 2021. SRNL-STI-2021-625.

Verst, C. 2022. Interim Irradiation and Measurement of As-dried, as-corroded and MURR Hydrated Oxide Specimens (Large Coupons). Savannah River National Laboratory, Tech. rep. SRNL-L3110-2022-00001.

Winston, P., Middlemas, S., Winston, A., Aguiar, J., Liu, X., Tolman, K. 2020. Aluminum Spent Fuel Performance in Dry Storage Task 4 Aluminum Oxide Sampling of ATR Dry Stored Fuel, Technical Report, Idaho National Laboratory, INL-EXT-20-58404, 2020.

Wittman, R., Hanson, B. 2015. Radiolysis model analysis for a used fuel storage canister. In proceedings: IHLRWM April 2015.

Westbrook, M.L., Sindelar, R.L., Fisher, D.L. 2015. Radiolytic hydrogen generation from aluminum oxyhydroxide solids: theory and experiment. J. Radioanal. Nucl. Chem., 303, pp 81-86.

Zalupski, P. 2018 Aluminum Clad Spent Nuclear Fuel Task 2: Oxide Layer Radiolytic Gas Generation Resolution Experiment Test Plan. Idaho National Laboratory, INL/EXT-18-45858.